Journal of Computational Electronics manuscript No.
(will be inserted by the editor)

Gate-induced carrier density modulation in bulk graphene: Theories and electrostatic simulation using MATLAB pdetool

Ming-Hao Liu (劉明豪)

Received: date / Accepted: date

Abstract Theories of the gate-induced carrier density modulation in bulk graphene are reviewed, and a numerical simulation procedure based on electrostatic simulation using Matlab's pdetool is introduced. A brief introduction to the usage of the tool aiming at the present electrostatic problem is introduced particularly for the readers who are as well Matlab users. The analytical capacitance models and the numerical simulation, namely the Poisson-Dirac iteration method, are compared, showing that the quantum capacitance correction plays usually a minor role. Practical examples corresponding to realistic experimental conditions for graphene *pnp* junctions, superlattices, and linear background potential are shown to illustrate the applicability of the introduced methods for calculating the carrier density modulation in bulk graphene.

PACS 73.22.Pr · 85.30.De · 72.80.Vp · 41.20.Cv

1 Introduction

Electronic transport in graphene [1,2], a one-atom-thick honeycomb carbon lattice, is one of its main issues among the increasing number of fundamental studies ever since the first successful isolation of stable monolayer graphene flakes in 2004 [3]. What led to the explosive growth of the graphene literature, however, was not only the discovery of the mechanical exfoliation (Scotch-tape method) for graphene flake preparation, which made graphene easily accessible to laboratories all over the world, but also the characterization of the electronic properties of graphene by electrical gating, which provides a direct way to modulate the carrier density, and hence the Fermi level, of graphene [3]. Conductance (resistance) sweep using a single backgate is therefore a standard electronic characterization tool for graphene. Double-gated graphene opens even more possibilities of graphene electronics and allows experimental studies of graphene *pn* and *pnp* junctions [4,5,6,7,8], as well as the interesting physics of Klein tunneling [9,10,11,12,13]. Gate-induced carrier density modulation therefore plays an essential role for fundamental as well as advanced studies of graphene electronics.

Theory of the gate-induced carrier density modulation is mainly an electrostatic problem. How one should obtain the gate-voltage dependence of the carrier density in graphene depends actually on how precise one wishes. For cheapest computation, the graphene sheet carrier density can be directly regarded as the induced surface charge density adjacent to graphene [3], which is treated as a conductor fixed at zero potential. This corresponds to the classical capacitance model (CCM) that is widely adopted in most experimental works on graphene transport [2] and can be solved exactly. A more precise computation takes into account the relation between the induced charge density on graphene and the electric potential energy that those charge carriers gain, through the graphene density of states [14,15,16]. This makes the computation iterative [8,17,18] and hence a bit more expensive, but actually corresponds to the quantum capacitance model (QCM) [19], where an exact solution for single-gated graphene is possible [16]. Further consideration such as the Coulomb interaction of the induced charges on the graphene sheet is possible [15,17], but this would be out of the scope of the present discussion.

Whereas a thorough and comprehensive review on the theory of gate-induced carrier density modulation of bulk graphene so far does not exist in the literature, the major part of this paper aims at providing this missing piece. The review includes both the analytical and numerical aspects, as

Ming-Hao Liu (劉明豪)
Institut für Theoretische Physik, Universität Regensburg,
D-93040 Regensburg, Germany
E-mail: minghao.liu.taiwan@gmail.com

well as a brief introduction to the usage of Matlab's pdetool, in order for a self-contained context. Readers who happen to be Matlab users would find this brief usage helpful, but non-Matlab users may as well neglect it without encountering further gaps. The analytics based on the CCM and QCM and the numerics based on the iterative method, namely, the Poisson-Dirac method (PDM), using Matlab's pdetool will be compared, showing that the quantum correction plays usually a minor role, unless the oxide between graphene and the metallic gate is exceedingly thin. In the case of single-gated graphene, consistency between the QCM and PDM is satisfactory even for nonuniform capacitors and becomes exact for uniform capacitors.

With a full understanding of the gate-voltage modulation of the graphene carrier density, examples of its applications aiming at providing realsitic local energy band offsets due to electric gating will be discussed. This is particularly important for an accurate computational modeling of transport in graphene. Examples include the cases of (i) a single graphene *pnp* junction, (ii) a graphene superlattice, and (iii) a background potential linear in position. Practically, the case of (i) provides the study of the physics of Klein backscattering [20,12,21], while the combination of the cases (ii) and (iii) is the underlying prerequisite of the Bloch-Zener oscillation in graphene [22].

This paper is organized as follows. In Sec. 2, we first provide a brief introduction to the usage of Matlab's pdetool, pointing out the least knowledge required to apply the tool on the present specific electrostatic problem. Theories of the gate-induced carrier density modulation in graphene are reviewed in Sec. 3, where the analytics based on the capacitance models and the numerics based on the PDM is also compared. Practical applications based on the theories reviewed in Sec. 3 are given in Sec. 4, and a summary of the present work is concluded in Sec. 5.

2 Usage of Matlab's pdetool for electrostatics

The pdetool is a useful numerical tool built in Matlab and provides a convenient way to solve several classic partial differential equation (PDE) problems in two-dimension. For the electrostatics at our present interest, the Poisson equation,

$$-\nabla\cdot(\varepsilon_r\nabla u)=\frac{\rho}{\varepsilon_0}, \tag{1}$$

obtained from two of the Maxwell's equations, $\nabla\times\mathbf{E}=0$ and $\nabla\cdot\mathbf{D}=\rho$, which respectively lead to $\mathbf{E}=-\nabla u$ and $\nabla\cdot\varepsilon_r\mathbf{E}=\rho/\varepsilon_0$, is the central equation that the pdetool solves for the electric potential u.[1] In Eq. (1), the product of the dielectric constant (relative permittivity) ε_r and the free space permittivity ε_0 gives the absolute permittivity $\varepsilon=\varepsilon_r\varepsilon_0$.

A full introduction to the usage of the pdetool can be found in the Matlab documentation [23] and need not be repeated here. To digest the full user's guide of the tool, however, is not necessary for our focussed problem, which is essentially an electrostatic problem. This section is basically to elaborate those that are less clear in [23] but nevertheless important for our purpose of obtaining the gate-voltage dependence of the graphene carrier density, and to point out the least required knowledge for this purpose.

2.1 Overview of pdetool

To solve a PDE problem using the pdetool, required necessary inputs can be exported from the graphical user interface (GUI) of the pdetool (initiated by executing "pdetool" from the command window) and are briefly described in the following.

(i) *System geoemtry*. The geometrical shapes of the building blocks, such as the oxide layers, metallic gates, etc., which constitute the system where the PDE problem is defined, can be drawn in the "Draw Mode" of the GUI. The resulted "decomposed geometry" allows us to proceed to the rest of the inputs, but there is no need to "Export Decomposed Geometry, Set Formula, Labels..." from the "Draw menu" since they will not be needed by the PDE solvers.

(ii) *PDE coefficients*. In the "PDE Mode" of the GUI, one can designate different regions of materials by filling in the respective dielectric constants and space charge densities. These are stored in certain PDE coefficients matrices, which can be output from the GUI and will be required by the PDE solvers in programming.

(iii) *Boundary conditions*. In the "Boundary Mode" of the GUI, boundary conditions for each bounding edge can be assigened. The resulting boundary matrix *b*, which will be required by the PDE solvers in programming, and the Decomposed Geometry, which will be required when visualizing the PDE geometry, can be exported from the "Boundary menu". An elaborated instruction about *b* will be given later.

(iv) *Mesh points*. The mesh points are those spatial points at which the numerical solutions are desired. They can be created, refined, or jiggled in the "Mesh Mode" of the GUI. The resulting triangular mesh data, stored by point, edge, and triangle matrices, can be exported by the GUI and will be used not only when calling for the PDE solvers but also when visualizing the solution.

With all these requirements completed, the PDE problem is then defined, and the solution can as well be obtained by clicking "Solve PDE" within the GUI, which is

[1] To be consistent with the pdetool, we name the electric potential as *u*, while reserve the variable *V* for the energy band offset (the "on-site energy" in the language of tight-binding formulation).

user-friendly but cannot be "programmed". When performing certain real calculations, however, especially when a systematic change of variables is required, programming with, e.g., looping, is inevitable and the requirements of (ii)–(iv) will be the necessary inputs of the PDE solvers. For our purpose of simulating the carrier density modulation due to gating, we would often need to change the gate voltages, which are described by the boundary conditions. Thus although each of (ii)–(iv) can be programmed by using relevant commands, in the following only the implementation of (iii) by commands will be described in detail.

2.2 Boundary conditions

2.2.1 The boundary condition matrix

By searching "assemb" from the Matlab help, we see that the boundary conditions are saved in a matrix called b, with the following data format:

- Row 1 contains the dimension N of the system. (Note: normally $N = 1$. If one solves two coupled variables, then $N = 2$, etc.; by examining the exported boundary condition matrix b, one woule find that $N = 0$ for inner boundaries.)
- Row 2 contains the number M of Dirichlet boundary conditions.
- Rows 3 to $3+N^2-1$ contain the lengths for the strings representing q. The lengths are stored in columnwise order with respect to q.
- Rows $3+N^2$ to $3+N^2+N-1$ contain the lengths for the strings representing g.
- Rows $3+N^2+N$ to $3+N^2+N+MN-1$ contain the lengths for the strings representing h. The lengths are stored in columnwise order with respect to h.
- Rows $3+N^2+N+NM$ to $3+N^2+N+MN+M-1$ contain the lengths for the strings representing r.
- The following rows contain *text expressions* representing the actual boundary condition functions.

Here, two types of boundary conditions[2] are included, namely, the Neumann boundary

$$\mathbf{n}\cdot(c\nabla u)+qu=g, \tag{2}$$

and the Dirichlet boundary

$$hu=r. \tag{3}$$

Here, c contains the PDE coefficients (such as the dielectric constant in different regions), and $\mathbf{n}$ is the normal of the boundary. So the boundary conditions for given gate voltages would be the Dirichlet type, with $h = 1$ and r being the corresponding voltage. For the Neumann type boundary condition, we normally consider $q = 0$, and g represents the surface charge.

In the following, let us be more specific about the format of the boundary conditions matrix, considering the two types of boundaries with $N = 1$.

2.2.2 Dirichlet boundary

The format of the boundary matrix b is described as follows.

- Row 1 contains the dimension N of the system: 1.
- Row 2 contains the number M of Dirichlet boundary conditions: 1.
- Row 3 contains the length for the strings representing q, which is 1 since $q = 0$, though not used.
- Row 4 contains the length for the strings representing g, which is 1 since $g = 0$, though not used.
- Row 5 contains the length for the strings representing h, which is 1 since $h = 1$.
- Row 6 contains the length for the strings representing r.
- Then comes the text expressions of q, g, h, r.

An example of a Dirichlet boundary with $r = 3.5$ would be:

```
b = [1 1 1 1 1 3 '0' '0' '1' '3.5']';
```

The boundary condition may include the x and y position coordinates and their functions, and can be written even in terms of the solution u (nonlinear solver required). For example,

```
b = [1 1 1 1 1 4 '0' '0' '1' 'x.^2']';
```

For another example,

```
b = [1 1 1 1 1 9 '0' '0' '1' 'sin(x).^u'];
```

2.2.3 Neumann boundary

The format of the boundary matrix b is described as follows.

- Row 1 contains the dimension N of the system: 1.
- Row 2 contains the number M of Dirichlet boundary conditions: 0.
- Row 3 contains the length for the strings representing q, which is 1 since $q = 0$.
- Row 4 contains the length for the strings representing g.
- Then comes the text expressions of q, g.

An example of a Neumann boundary with surface charge $g = 1.6$ would be

```
b = [1 0 1 3 '0' '1.6']';
```

Another example

```
b = [1 0 1 21 '0' '-13.295*sign(u).*u.^2']';
```

will actually be used when we apply the Poisson-Dirac iteration method.

[2] The mixed type boundary conditions will not be encountered in the present discussion.

2.2.4 Text expression of the boundary conditions

The boundary condition matrix *b* exported from the GUI of the pdetool looks filled with purely numbers. This is the "number representation" of the text strings. For example, a number 48 within the *b* matrix actually means '0':

```
>> char(48)

ans =

0
```

Conversely, if we want to transform the strings into numbers, we can simply use the 'double' command:

```
>> double('x.^2')

ans =

   120    46    94    50
```

Thus to enter a boundary condition of, e.g., $-(x^2+y^2)$, we may fill in:

```
double('-(x.^2+y.^2)')'
```

To enter a Dirichlet boundary condition of a given number assigned by a variable named `Vtg`, we may fill in:

```
double(num2str(Vtg))'
```

Note that in the above two examples, the operator `'` at the end is to take transpose of the converted text strings since the boundary conditions are saved columnwise in *b*.

For a real PDE problem, the number of columns of the *b* matrix depends on the total number of edges, including inner and outer boundaries. The *n*th column records the boundary condition for the *n*th edge. Thus before exporting the initial *b* matrix from the GUI of pdetool, one has to check the corresponding boundary label (by showing the edge labels in the "Boundary Mode").

2.3 Some important commands

2.3.1 Solving the PDE

A standard PDE solver is called `assempde`. An example for its usage is as follows.

```
u = assempde(b,p,e,t,c,a,f);
% b: matrix of boundary conditions
% p: points of the mesh grid
% e: edges
% t: triangles
% c,a,f: coefficients of the pde problem
```

When the solution is involved in the boundary conditions, the solution mode has to be switched to nonlinear. An example for its usage is as follows.

```
[u,res] = pdenonlin(b,p,e,t,c,a,f, ...
    'report','on','MaxIter',1e5,'u0',u0);
% u: the solution, res: not important here
% p,e,t,c,a,f: same as above
% 'MaxIter': maximal number of iter. rounds
% 'u0': initial guess of the solution
```

2.3.2 Interpolation

To find the values at those points one desires, an important command called `tri2grid` should be used, which interpolates from the PDE triangular mesh to a given rectangular grid. An example for usage is as follows.

```
uxy = tri2grid(p,t,u,x,y);
% u: the obtained solution
% p,t: same as above
% x,y: rectangular grid points for interpol.
```

2.4 Remarks on units

In the pdetool, everything is displayed with dimensionless numbers. The actual units can be chosen as what we would like. Deducing relevant coefficients for a specific set of chosen units is therefore important before we use the pdetool to solve any actual problems.

In addition to the physical units, the free space permittivity ε_0 is suppressed throughout the program. Recall the boundary conditions for the displacement field D at a conductor-dielectric boundary, which can be derived by applying the Gauss's law: $D_t = 0$ and $D_n = \rho_s$, where D_t and D_n represent the components tangential and normal to the interface, respectively. The normal component of the displacement field D_n therefore means the surface charge density:

$$-\varepsilon_r \nabla u \cdot \mathbf{n} = \frac{\rho_s}{\varepsilon_0}. \tag{4}$$

Comparing Eq. (4) with Eq. (2) with $q = 0$ and c representing ε_r (instead of ε), one can see that the "Surface charge" actually means

$$g = \frac{\rho_s}{\varepsilon_0}, \tag{5}$$

when filling the Neumann boundary condition in the "Boundary Mode" of the GUI. Similarly, when filling the PDE coefficients in the "PDE Mode", the "Space charge density" actually means `rho` $= \rho/\varepsilon_0$, i.e., the right-hand side of Eq. (1).

3 Theories of gate-induced carrier density modulation

In this section, analytical theories of the gate-induced carrier density modulation, including the classical and quantum capacitance models, are briefly reviewed, a numerical scheme of the Poisson-Dirac iteration method is introduced, and a numerical comparison between analytics and numerics is provided.

3.1 Classical capacitance model

3.1.1 The model

We begin with the classical capacitance model, which considers a parallel-plate capacitor composed of an oxide dielectric with permittivity ε sandwiched by a metallic gate (at $z = d$) and a conducting graphene sheet (at $z = 0$) as sketched in Fig. 1(a). Let the electric potential at the gate be $u(x,z = d) = V_g$ and the graphene layer be grounded: $u(x,z = 0) = V_G = 0$. The surface charge density at $z = 0^+$ (the surface of the oxide dielectric in contact with the graphene layer) from Eq. (4) is given by

$$\rho_s = -\varepsilon \left.\frac{\partial u}{\partial z}\right|_{z=0^+} = -\varepsilon \frac{V_g - 0}{d - 0} = -C_{\rm ox} V_g, \tag{6}$$

where $C_{\rm ox} = \varepsilon/d$ is the classical capacitance (per unit area) of a uniform parallel-plate capacitor. Regarding this surface charge (6) directly as those in the graphene layer, we have the carrier density

$$n_C = \frac{\rho_s}{-e} = \frac{C_{\rm ox}}{e} V_g, \tag{7}$$

which is a widely used formula for estimating the graphene carrier density [2]. For uniform capacitors with $C_{\rm ox} = \varepsilon/d$, Eq. (7) numerically reads

$$n_C = \frac{\varepsilon V_g}{ed} = \frac{\varepsilon_r V_g}{d} \times 5.5263 \times 10^{12}\,{\rm cm}^{-2}, \tag{8}$$

where V_g and d are in units of V and nm, respectively.

3.1.2 Using pdetool

The Dirichlet boundary conditions

$$u(x,z) = \begin{cases} 0, & \text{at graphene boundary} \\ V_g, & \text{at gate boundary} \end{cases} \tag{9}$$

can be straightforwardly implemented.[3] The standard PDE solver `assempde` introduced in Sec. 2.3 should be chosen.

[3] If a uniform capacitor (without x dependence) is desired, one needs to assign Neumann boundary conditions at the left and right sides of the oxide boundaries with vanishing surface charge density $g = 0$, which forces the displacement field to be normal (tangential) to the side (top and bottom) boundaries.

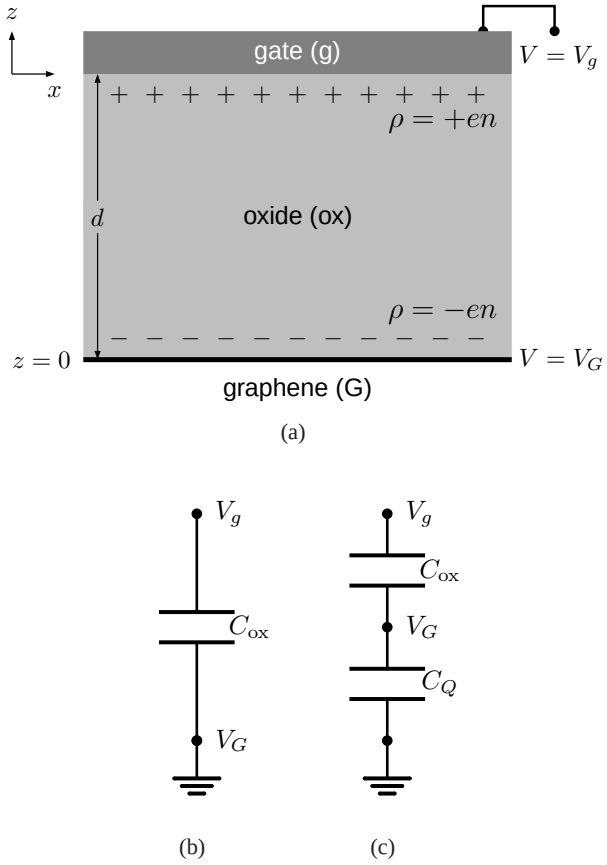

Fig. 1 (a) Schematic of a single-gated graphene. (b) Equivalent circuit plot of the classical capacitance model. (c) Equivalent circuit plot of the quantum capacitance model.

Working with units V and nm, the carrier density (7) is numerically given by

$$n_C(x) = \varepsilon_r \left.\frac{\partial u(x,z)}{\partial z}\right|_{z=0} \times 5.5263 \times 10^{12}\,{\rm cm}^{-2}. \tag{10}$$

Note that the interpolation command `tri2grid` introduced in Sec. 2.3 may be useful in performing the numerical derivative $\partial u/\partial z$ at $z = 0$.

3.1.3 Remark on the gate-induced Rashba spin splitting

At this stage we may also estimate for graphene the gate-induced Rashba spin splitting, an intrinsic coupling between the spin and orbital degrees of freedom of charge carriers in a two-dimensional conducting plane subject to a perpendicular electric field [24,25]. In graphene, the Rashba spin splitting has been shown by first principles to exhibit a linear dependence on the electric field [26,27]: $\Delta_R \approx 0.01\,|E|\,{\rm meV}$, where E is the electric field strength perpendicular to graphene given in units of V / nm. If the graphene carrier density n stems from gating, the corresponding surface charge density $|\rho_s| = e|n| = \varepsilon|E|$, in fact, has already

revealed the displacement field on itself, allowing us to express the Rashba spin splitting in terms of the carrier density,

$$\Delta_R = \frac{n}{\varepsilon_r} \times 1.8095 \times 10^{-6}\text{eV}, \tag{11}$$

where n is in units of $10^{12}\,\text{cm}^{-2}$, a typical order of the graphene carrier density.

This estimation indicates that the Rashba spin splitting induced solely by electric gating typically lies in the order of μeV, which may hinder the observation of those interesting physics based on the Rashba spin-orbit coupling in graphene, such as the interfacial spin and charge currents [28,29], or the spin-dependent Klein tunneling [30,31]. The position dependence of the Rashba coupling across a *pn* junction interface [32], on the other hand, can be accurately taken into account by putting the x-dependence of n (or even ε_r) in Eq. (11). A stronger Rashba spin splitting in graphene is therefore less possible by gating, but may be achieved by, for example, using a ferromagnetic substrate with an intercalated gold monolayer [33].

3.2 Poisson-Dirac iteration method

From Eq. (6) to Eq. (7), the assumption that "the induced surface charge density at the dielectric surface is the graphene carrier density" obviously have neglected a few physical details, such as the graphene density of states that govern the statistics of how the states in graphene should be filled by the carriers accordingly. In addition, filling the carriers into graphene causes the change of its Fermi level, implying a potential energy shift that should further correspond to the electric potential times the electron charge. These are what the classical capacitance model have neglected and what the following Poisson-Dirac iteration method is going to compensate.

3.2.1 Basic idea

Consider a pristine graphene with Fermi level lying exactly at the charge neutrality point, i.e., the Dirac point $E_F = 0$. Application of the gate voltage V_g induces a certain amount of additional charges on graphene, $\rho_s = -en$, which occupy the states in graphene according to its density of states $D(E) = 2|E|/\pi(\hbar v_F)^2$ (within the Dirac model):

$$n(E) = \int_{-\infty}^{E} D(E')dE' = \text{sgn}(E)\frac{1}{\pi}\left(\frac{E}{\hbar v_F}\right)^2, \tag{12}$$

where $v_F \approx 10^8\,\text{cm}/\text{s}$ is the Fermi velocity in graphene. A positive (negative) electron number density n raises (lowers) the Fermi level from 0 to E. On the other hand, the electron at the Fermi level, which is responsible for transport in the linear response regime, gains an energy $-eV_G$ from the electric field, where $-e$ is the electron charge[4] and V_G is the electric potential at the graphene sheet obtained by solving the Poisson Eq. (1). This potential energy $-eV_G$, which is equivalent to the "on-site energy" in the tight-binding transport formulation (see, for example, [21]), will raise the whole band structure, and thus lower the Fermi level by the same amount. We can therefore legitimately put

$$E = -(-eV_G) = +eV_G \tag{13}$$

into Eq. (12), leading to

$$\frac{\rho_s}{\varepsilon_0} = \frac{-en}{\varepsilon_0} = -\frac{e}{\varepsilon_0}\,\text{sgn}(V_G)\frac{(eV_G)^2}{\pi(\hbar v_F)^2}. \tag{14}$$

The surface charge density at the graphene layer is now expressed in terms of the solution $u(x, z = 0)$, but is at the same time the Neumann boundary condition that influences the numerical solution to the Poisson equation. This formally makes the solution process iterative.

3.2.2 Using pdetool

The Dirichlet boundary condition (9) for the gate boundary remains valid, while that for the graphene boundary has to be modified to the Neumann type:

$$u(x,z) = \begin{cases} g, & \text{at graphene boundary} \\ V_g, & \text{at gate boundary} \end{cases}, \tag{15}$$

where $g = \rho_s/\varepsilon_0$ is given by Eq. (14). Working with units V and nm together with $v_F = 10^8\,\text{cm}/\text{s}$, Eq. (14) becomes

$$\frac{\rho_s}{\varepsilon_0} = -13.295\,\text{sgn}(V_G)\left(\frac{V_G}{\text{V}}\right)^2\frac{\text{V}}{\text{nm}}, \tag{16}$$

which should be keyed as "`-13.295*sign(u).*u.^2`" in the boundary condition matrix, noting that the solution in the pdetool is by default named u. The nonlinear solver `pdenonlin` introduced in Sec. 2.3 has to be chosen in this case, where the solution is involved in the boundary conditions, and the iteration will be automatically processed by the pdetool.

Once the solution $u(x,z)$, and hence the electrostatic potential at the graphene layer $V_G(x) = u(x, z = 0)$, is iteratively obtained, the desired carrier density profile $n(x)$ can then be expressed in terms of $V_G(x)$:

$$n_{\text{PD}}(x) = 7.3471 \times 10^{13} \times \text{sgn}[V_G(x)]\left[\frac{V_G(x)}{\text{V}}\right]^2 \text{cm}^{-2}, \tag{17}$$

which follows from Eqs. (12) and (13). Note that we have added explicitly a subscript PD in Eq. (17) to distinguish with the classical contribution, n_C.

[4] Throughout this paper, $e = 1.60217733 \times 10^{-19}$ C is the elementary positive charge.

3.3 Quantum capacitance model

The relation between the induced charge density on graphene and the electric potential energy that those charge carriers gain through the graphene density of states is taken into account in the PDM, with a price of iteration process paid. For single-gated graphene, there is an alternative that can take this into account analytically: the quantum capacitance model [19], which we briefly review here for bulk graphene following the work of [16].

3.3.1 The model

The single-gated graphene shown in Fig. 1(a) is treated by the equivalent circuit plot as shown in Fig. 1(c), where an additonal capacitor C_Q is inserted between the voltage point V_G and the ground, as compared with the CCM, Fig. 1(b). As Fig. 1(c) suggests $V_g = V_G + V_{\rm ox}$, using $C_{\rm ox} = |\rho|/V_{\rm ox} = en/V_{\rm ox}$ we have

$$V_g = V_G + \frac{en}{C_{\rm ox}} \implies n = \underbrace{\left(\frac{C_{\rm ox}}{e}V_g\right)}_{\text{classical}} + \underbrace{\left(-\frac{C_{\rm ox}}{e}V_G\right)}_{\text{quantum}}. \tag{18}$$

Following the same physics stated in Sec. 3.2.1, the carrier density at the graphene layer, i.e, Eq. (14) divided by $-e$, is expressed in terms of the electric potential thereof as

$$n = \mathrm{sgn}(eV_G)\frac{1}{\pi}\left(\frac{eV_G}{\hbar v_F}\right)^2. \tag{19}$$

Equating (18) and (19), one obtains a quadratic equation for V_G,

$$\mathrm{sgn}(eV_G)\frac{1}{\pi}\left(\frac{eV_G}{\hbar v_F}\right)^2 = \frac{C_{\rm ox}}{e}V_g - \frac{C_{\rm ox}}{e}V_G. \tag{20}$$

Solving Eq. (20) for V_G and putting back to Eq. (18), the graphene carrier density can be written as

$$n = n_C + \Delta n, \tag{21}$$

where n_C given by Eq. (7) is the classical contribution, and

$$\Delta n = n_Q\left(1 - \mathrm{sgn}(n_C)\sqrt{1 + 2\frac{|n_C|}{n_Q}}\right) \tag{22}$$

with

$$n_Q = \frac{\pi}{2}\left(\frac{C_{\rm ox}\hbar v_F}{e^2}\right)^2 \tag{23}$$

corresponds to the quantum correction.[5]

[5] Note that Eqs. (21)–(23) were first derived in [16] and reviewed in [2], but a factor of 2 in the square root of Eq. (22) corresponding to the formula (1.15) in [2] was missing.

3.3.2 Quantum correction for uniform capacitors

For uniform capacitors, the well-known oxide capacitance is given by $C_{\rm ox} = \varepsilon/d$, or, by definition written as

$$C_{\rm ox} = \frac{e\cdot n_C}{V_g}, \tag{24}$$

such that Eq. (23) and hence the quantum correction (22) is solely determined by the classical contribution n_C. In this case we can further express Eq. (23) as $n_Q = (\varepsilon_r/d)^2 \times 2.0784\times 10^{11}\,\mathrm{cm}^{-2}$, where d is in units of nm and $v_F = 10^8\,\mathrm{cm/s}$ is again adopted. Together with Eq. (8), the quantum correction given by Eq. (22) can be written as

$$\Delta n = \mathrm{sgn}(V_g)\left(\frac{\varepsilon_r}{d}\right)^2\left(1 - \sqrt{1 + 53.178\frac{|V_g|\,d}{\varepsilon_r}}\right), \times 2.0784\times 10^{11}\,\mathrm{cm}^{-2} \tag{25}$$

where V_g is in units of V. We will soon see that this analytical QPM for a uniform capacitor will exactly correspond to the numerical PDM. With nonzero V_g and large d, one can further approximate Δn as

$$\Delta n \approx -\mathrm{sgn}(V_g)\left(\frac{\varepsilon_r}{d}\right)^{3/2}\sqrt{|V_g|}\times 1.5156\times 10^{12}\,\mathrm{cm}^{-2}, \tag{26}$$

which implies a rapid decay of Δn with d.

3.3.3 Remark on quantum capacitance

Note that the appearance of C_Q stems from the finite density of states provided by the conducting layer for the electrons to occupy following the quantum nature of the Pauli exclusion principle, and hence the name quantum capacitance [19], which is not restricted to the material graphene. The expression of C_Q for graphene [16], however, is not important for the present discussion. Instead, C_Q leads to a quantum correction to the gate-induced carrier density Δn, which is the main focus here.

In addition, recent experimental progress on the measurement of graphene quantum capacitance [34,35,36] suggests that the electron-hole puddles [37] induced by charged impurities may influence C_Q at energies close to the charge neutrality point. The corresponding carrier density fluctuation δn, which can be considered to develop a microscopic model to account for the smoothing of the graphene quantum capacitance at the charge neutrality point [38], is beyond the scope of the present discussion.

3.4 Analytics vs numerics

The two analytical capacitance models and the numerical scheme of the Poisson-Dirac iteration method are compared in the following, considering a single-gated graphene with individually infinite and finite sizes of the gate.

We start with a uniform capacitor with infinitely extending parallel conductors with different spacings $d = 100, 200, 300$ nm. The oxide dielectric is regarded as SiO_2 with $\varepsilon_r = 3.9$. The classical contribution n_C is first computed following Sec. 3.1.2 [which gives the same result with Eq. (8)], and the quantum correction Δn is computed in two ways. For the analytical QCM, Eq. (25) is used to compute Δn. For the numerical PDM, the full carrier density $n_{\rm PD}$ is computed following Sec. 3.2.2, and the correction is given by the difference $n_{\rm PD} - n_C$. As shown in Fig. 2, the correspondence between the two approaches is exact.

Next we consider a finite-size suspended topgate (such as those fabricated in [7]) with various voltages $V_{\rm tg} = 5, 10, 15\,\mathrm{V}$ and an extremely narrow spacing $d = 20$ nm. The calculations are similar to those for the uniform case described above. The only difference is the approximating form of the dielectric capacitance,

$$C_{\rm ox}(x) \equiv \frac{e \cdot n_C(x)}{V_{\rm tg}}, \tag{27}$$

from which n_Q given by Eq. (23) and hence the quantum correction Eq. (22) from the analytical QCM is obtained. The total carrier densities calculated by the iterative PDM, $n_{\rm PD}$, and that by the QCM, $n_{\rm QC}$, are compared in the left panel of Fig. 3; the difference can hardly be told. In the right panel of Fig. 3, the total carrier density is compared with the classical contribution n_C; the difference is merely moderate, implying that n_C is still the main contribution to the gate-induced carrier density. The quantum corrections from the two approaches are compared in Fig. 4, where a clear but still moderate discrepancy can be seen.

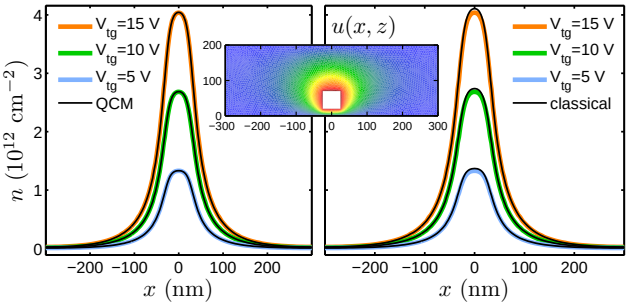

Fig. 3 Left: Comparison between the position-dependent total carrier density obtained from the Poisson-Dirac method $n_{\rm PD}(x)$ and that from the quantum capacitance model $n_{\rm QC}(x)$, at various topgate voltages. Right: Total carrier density $n_{\rm PD}(x)$ vs the classical contribution $n_C(x)$. Inset: Spatial distribution of the electric potential $V(x,z)$ due to the presence of the topgate with cross section 50 nm $\times$50 nm suspended 20 nm above the graphene sheet. The length unit is nm.

Fig. 3 Left: Comparison between the position-dependent total carrier density obtained from the Poisson-Dirac method $n_{\rm PD}(x)$ and that from the quantum capacitance model $n_{\rm QC}(x)$, at various topgate voltages. Right: Total carrier density $n_{\rm PD}(x)$ vs the classical contribution $n_C(x)$. Inset: Spatial distribution of the electric potential $V(x,z)$ due to the presence of the topgate with cross section 50 nm $\times$50 nm suspended 20 nm above the graphene sheet. The length unit is nm.

From the above testing calculations, we may conclude that the classical contribution n_C always plays the dominant role, and the QCM is equivalent to the PDM in the case of uniform capacitors. For nonuniform capacitors, the approximation of Eq. (27) that is generalized from Eq. (24) allows the non-iterative QCM to work equally well as compared to the iterative PDM, for the case of single- and finite-gated graphene.

3.5 Beyond single gating

The above discussion considers only a single-gated graphene. For double-gated graphene with topgate and backgate at two sides of the graphene layer, the two gates can be regarded as independent, and their contributions to the carrier density modulation can be treated separately. When

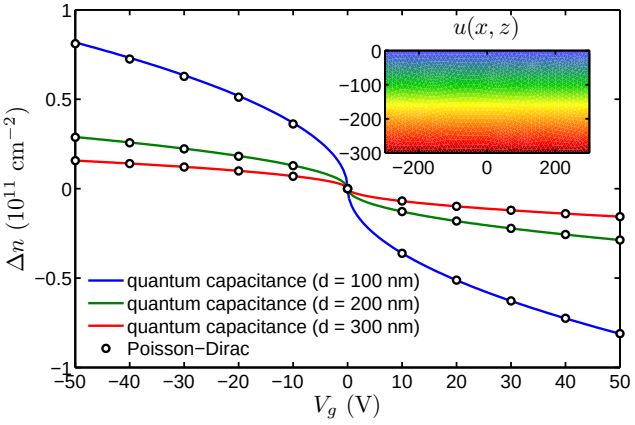

Fig. 2 The quantum correction to the gate-induced carrier density on graphene, calculated by the analytical quantum capacitance model and the numerical Poisson-Dirac iteration method. Inset: Two-dimensional plot for the iterative solution $u(x,z)$ with length unit nm.

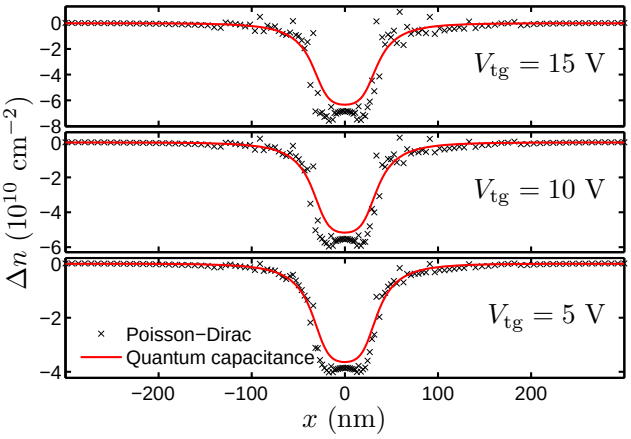

Fig. 4 Comparison of the correction to the carrier density from the Poisson-Dirac method, $n_{\rm PD}(x) - n_C(x)$, and that from the quantum capacitance model, $\Delta n(x)$ from Eq. (22), at various topgate voltages.

multiple gates are fabricated at the same side, however, such as using an embedded local gate in addition to a global backgate to creat ballistic *pnp* junction [13] (see Sec. 4.2), or patterned topgates that may generate a graphene superlattice (see Sec. 4.3), they should be simultaneously treated.

In fact, the CCM (Sec. 3.1.2) as well as the PDM (Sec. 3.2.2) are not restricted to the case of single-gated graphene. These two approaches work for any kind of gating geometry, provided that the boundary conditions [Eq. (9) for CCM and Eq. (15) for PDM] at the graphene layer are properly assigned. The applicability of the QCM (at the level that we introduced above), however, depends then on the gating geometry. In certain cases where Eq. (27) becomes ill-defined, the model cannot be simply applied. Generalization of the model to take into account composite gating geometry is possible, but is beyond the scope of the present discussion.

4 Applications

A successful simulation for electronic transport in bulk graphene relies on not only sophisticated computation techniques but also a realistic "potential profile" V that is experimentally relevant [21]. The term "potential" refers to the local potential energy added to the system Hamiltonian when modeling for graphene electronic transport. Thus the potential profile simply means the local energy band offset of the graphene sheet subject to a spatially varying carrier density due to electrical gating. This section is devoted to the application of the carrier density calculation: the corresponding potential profile, or the local energy band offset, which is a simple computational task but nevertheless important for graphene electronic transport calculations. A few concrete examples will be illustrated, after a short review of the potential profile is given.

4.1 Potential profile (local energy band offset)

In Sec. 3 we have introduced how to compute with a satisfactory accuracy the graphene carrier density n, which is related to the quasi-Fermi level through Eq. (12) as $E_F = \mathrm{sgn}(n)\hbar v_F\sqrt{\pi|n|}$. The energy band offset then reads $V = E_F^0 - E_F$, where E_F^0 is the global Fermi level. Choosing $E_F^0 = 0$ (as is usually the case and will be adopted in the rest of the calculations), the space-resolved band offset reads [21]

$$V(x) = -\mathrm{sgn}[n(x)]\hbar v_F\sqrt{\pi|n(x)|} = -11.667\times\mathrm{sgn}[n(x)]\sqrt{\frac{|n(x)|}{10^{10}\,\mathrm{cm}^{-2}}}\,\mathrm{meV}, \tag{28}$$

which is termed on-site energy in the tight-binding formulation for transport calculations.

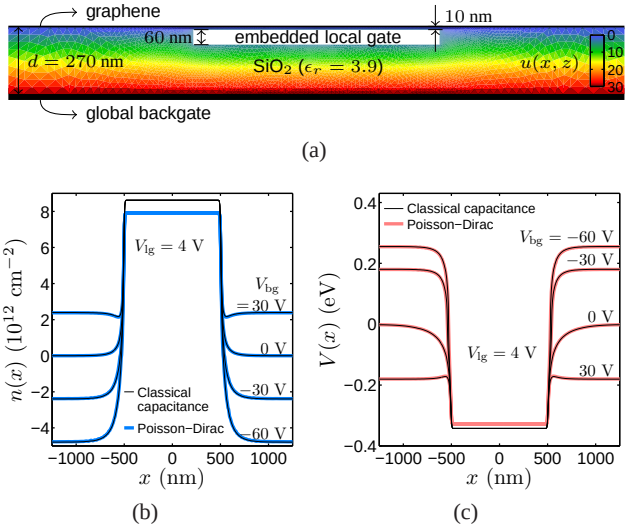

Fig. 5 A graphene *pnp* junction using a global backgate with various voltages V_{bg} and an embedded local gate fixed at $V_{\mathrm{lg}} = 4$ V. (a) The iterative solution $u(x,z)$ in units of V to the electrostatic potential within the oxide, subject to $V_{\mathrm{bg}} = 30$ V. The induced graphene carrier densities (b) and the corresponding potential profiles (c) based on the classical capacitance model and the Poisson-Dirac method.

It should be remarked that the Poisson-Dirac iterative solution to the electric potential at the graphene layer V_G times $-e$ readily gives the desired energy band offset, and Eq. (28) is not needed within this approach. Within the capacitance models, however, the electric potential on graphene is fixed at zero as a Dirichlet boundary condition, and Eq. (28) is needed. In other cases where PDM is partly used but the total carrier density is separately computed, one needs Eq. (28) as well.

4.2 Graphene *pnp* junctions

We begin the illustrative examples with a graphene *pnp* junction, using a global backgate and an embedded local gate. The gating geometry is sketched in Fig. 5(a), simular to those experimentally fabricated in [13]. In this case both of the global and local gates influence the graphene carrier density from the same side, and therefore have to be treated at the same time. The QCM does not apply here since Eq. (27) is ill-defined, but nevertheless can be used to estimate the quantum correction due to the embedded local gate at the region close to it. We will mainly compare the results from the CCM and those from the PDM, fixing the local gate voltage at $V_{\mathrm{lg}} = 4\,\mathrm{V}$ while varying the backgate voltage with $V_{\mathrm{bg}} = -60, -30, 0, 30\,\mathrm{V}$.

The computed carrier densities are shown in Fig. 5(b), where the Poisson-Dirac solution agrees well with the simulation presented in [13]. Since the local gate is embedded only 10 nm below the graphene sheet, the quantum correction excluded in the CCM becomes pronounced within

the locally gated region, and can be estimated by Eq. (25) of the QCM. At the center of the locally gated region, the electric field generated by the backgate is almost completely screened, and the classical contribution to the carrier density can be estimated by $n_C(x=0)=\varepsilon V_{\rm lg}/ed=8.621\,1\times10^{12}\,{\rm cm}^{-2}$, leading to $n_Q=3.161\,2\times10^{10}\,{\rm cm}^{-2}$ and hence $\Delta n=-7.073\,5\times10^{11}\,{\rm cm}^{-2}$, which is prettey close to $n_{\rm PD}(x=0)-n_C(x=0)=-7.0746\times10^{11}\,{\rm cm}^{-2}$ from the data of Fig. 5(b) for all $V_{\rm bg}$.

The carrier density profiles $n(x)$ of Fig. 5(b) are translated into $V(x)$ via Eq. (28), as shown in Fig. 5(c). The positive $V_{\rm lg}$ charges the locally gated graphene with a positive number of electrons, forming an n-type region with positive quasi-Fermi level $E_F(x)>0$ that is equivalent to applying a negative energy band offset $V(x)<0$. Outside the locally gated region, the carrier type of graphene is controled by the backgate with a similar principle. The most interesting feature here is that the locally gated region can be controled independently due to the screening of the embedded local gate, as is evident in both Figs. 5(b) and 5(c). This independent control leads to the four quadrants of the conductance map with the two boundaries perpendicular to each other [13], as contrary to those observed in top-gated devices [4, 5, 6, 7, 8, 11, 12].

4.3 Graphene superlattices

Next we turn to the possibility of generating a graphene superlattice by fabricating a series of patterned topgates. As sketched in Fig. 6(a), the PDE problem is defined within the region above the graphene sheet in order to solve the electric potential due to the topgates with various voltages $V_{\rm tg}=-5,-3,\cdots,5\,{\rm V}$. The contribution from the backgate is assumed to be uniform and can be treated independently. The strategy here is to compute first the carrier densities due to topgates, and then include the backgate contribution to yield the total carrier density that finally gives the energy band offset profile from Eq. (28). In this case the approximation (27) is rather acceptable, taking the voltage difference simply as $V_{\rm tg}$ fixed as position-independent. Hence we will compare the results from all of the three approaches.

The computed carrier densities, $n_{\rm PD}$ by PDM, $n_{\rm QC}$ by QCM, and n_C the classical contribution, are shown in Fig. 6(b). The curves of $n_{\rm PD}$ and $n_{\rm QC}$ almost coincide with each other. The relatively thick 40 nm of Al_2O_3 suppresses the quantum correction to a reasonably small amount, such that here the CCM is not a bad approximation, either. The discrepancy between n_C and $n_{\rm PD}$ (or $n_{\rm QC}$) is less pronounced at the regions between each adjacent pair of topgates since the quantum correction $|\Delta n|$ roughly decreases with the $3/2$-th power of the distance to the gate, as mentioned in Eq. (26).

The carrier density modulation follows the patterned topgates with a periodicity of 100 nm, giving rise to a periodic potential profile $V(x)$ as shown in Fig. 6(c), where a backgate contribution with $V_{\rm bg}=30\,{\rm V}$ is taken into account. Since $V(x)$ is related to $n(x)$ through a square-root relation, Eq. (28), the shape of $V(x)$ can be a bit different from that of $n(x)$, which is similar to a sine-like wave, especially for those $V(x)$ that alternate between positive and negative values. Note that the backgate voltage chosen in Fig. 6(c) results in a rather symmetric $V_{\rm tg}=-3\,{\rm V}$ curve since the corresponding carrier density $n(x)$ alternates symmetrically between positive and negative. In general, the alternation of $n(x)$ is not necessarily symmetric (about the charge neutral-

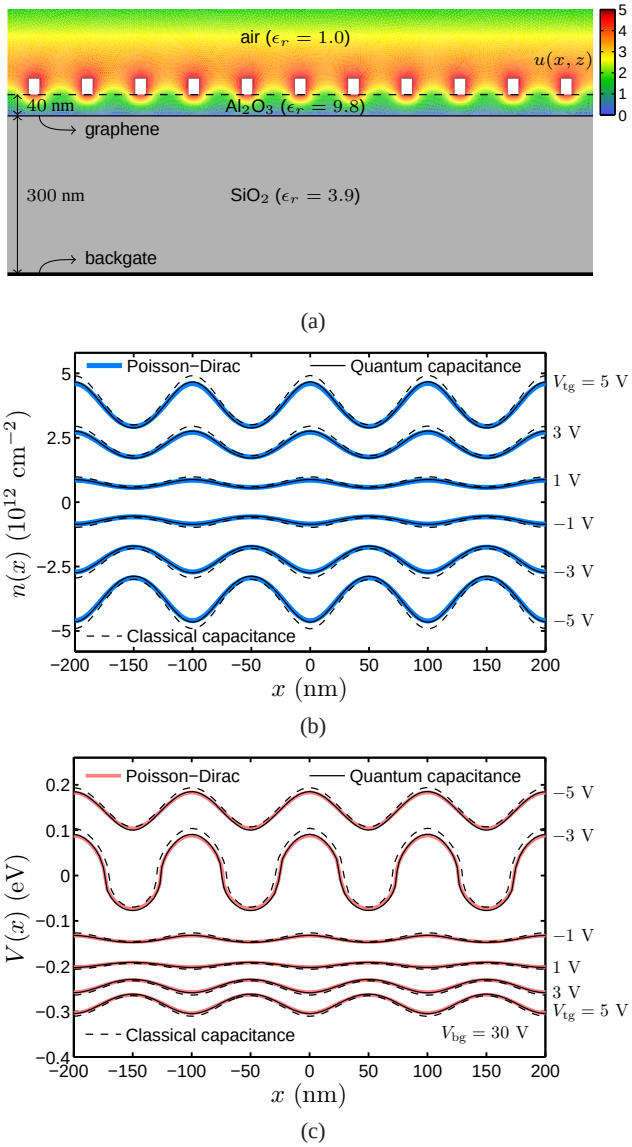

Fig. 6 Formation of a graphene superlattice using a series of patterned topgates and a global backgate, which are treated separately. (a) Iterative solution $u(x,z)$ with $V_{\rm tg}=5$ V, considering only the topgates. (b) The corresponding carrier densities based on all of the three approaches. (c) The profiles of the energy band offset from the total carrier density composed of the patterned topgates and the uniform backgate contributions.

ity point $n = 0$), and the resulting $V(x)$ profile can be of peculiar shapes.

4.4 Linear potential

In the previous example, we have demonstrated that fabricating a series of patterned topgates may generate a periodic potential, which, combined with a potential linear in position, forms the prerequisite of observing the Bloch-Zener oscillation in graphene [22]. In the last demonstrating example here, we point out a simple way to generate the linear potential: using a tilted backgate. As sketched in Fig. 7(a), where we consider a position-varying thickness of SiO_2 with a slope of $s = 0.05$ (an increase of 50 nm per micron). In this case the quantum correction does not play a role, and we show in Fig. 7(b) only the carrier densities from the CCM and the PDM, which coincide to each other.

Since the classical capacitance model works well here, with the oxide thickness $d(x) = d_0 + sx$, where $d_0 = 300\,\text{nm}$ is the thickness at the center, we can describe the carrier density as $n(x) = \varepsilon V_g / e(d_0 + sx)$ and hence the potential as $V(x) = -\operatorname{sgn}(V_g)\hbar v_F \sqrt{\pi\varepsilon\,|V_g|\,/e(d_0+sx)}$. The slope of the potential at $x = 0$, $dV(x)/dx|_{x=0}$, together with the intercept $V(x = 0)$, allows us to approximate the potential with a linear model,

$$
\begin{aligned}
V(x) &\approx V_0 + Sx \\
V_0 &= -\operatorname{sgn}(V_g)\sqrt{\frac{\varepsilon_r\,|V_g|}{d_0}} \times 0.27425\,\text{eV} \\
S &= \operatorname{sgn}(V_g)\frac{s\sqrt{\varepsilon_r\,|V_g|}}{d_0^{3/2}} \times 0.13713\,\text{eV nm}^{-1}
\end{aligned}
\qquad (29)
$$

In Fig. 7(c), we plot the potential profiles obtained from n_{PD} and from the linear model given by Eq. (29); the consistency is almost perfect.

5 Summary

In conclusion, theories of the gate-induced carrier density modulation in bulk graphene have been reviewed, including the classical capacitance model that most of the time plays the dominant role, the Poisson-Dirac method that takes into account the quantum correction by paying the price of iteration, and the quantum capacitance model that can analytically deal with the quantum correction. The analytical QCM and the numerically iterative PDM are shown to be exactly equivalent to each other for the uniform capacitor case. For the case of nonuniform capacitors, the QCM is also shown to work equally well with PDM, as long as the approximation (27) is not ill-defined. Along with the brief summary for

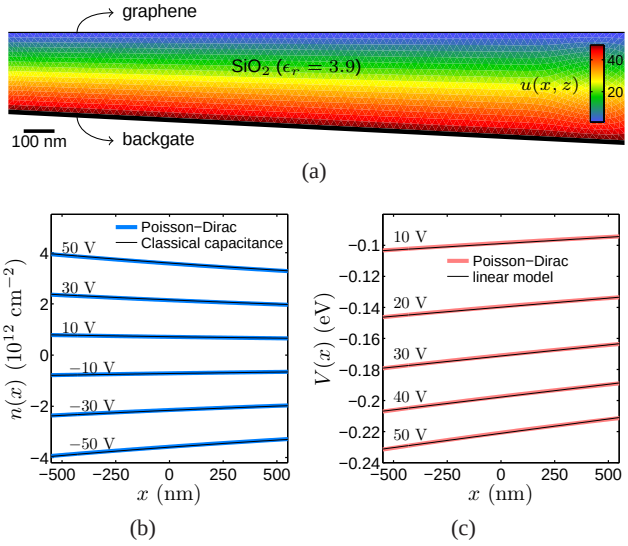

Fig. 7 (a) Electrostatic potential $u(x,y)$ inside a trapezoidal oxide layer. The tilted backgate with a slope of 0.05 generates a carrier density (b) that varies almost linearly with position. The corresponding potential profiles (c) also exhibit a linear behavior.

the usage of the Matlab pdetool, the major part of this work provides a self-contained instruction to calculating the carrier density of bulk graphene subject to any kind of gating geometry.

To demonstrate the application of the gate-induced carrier density modulation in graphene, practical examples have been illustrated, including the graphene *pnp* junction by using an embedded local gate in additional a global backgate [13], graphene superlattice potential by a series of patterned topgates, and the quasi-linear potential by using a tilted backgate. These examples correspond to the experimental conditions that provide a flexible platform to test the physics of Klein backscattering [20,12,21] and the Bloch-Zener oscillation [22] in graphene.

Acknowledgements The author thank T. Fang and D. Jena for their illuminating suggestions and F.-X. Schrettenbrunner and J. Eroms for helpful discussions. Financial support from Alexander von Humboldt Foundation is gratefully acknowledged.

References

1. A. H. Castro Neto, F. Guinea, N. M. R. Peres, K. S. Novoselov, and A. K. Geim, "The electronic properties of graphene," *Rev. Mod. Phys.*, vol. 81, p. 109, 2009.
2. S. Das Sarma, S. Adam, E. H. Hwang, and E. Rossi, "Electronic transport in two-dimensional graphene," *Rev. Mod. Phys.*, vol. 83, pp. 407–470, May 2011.
3. K. S. Novoselov, A. K. Geim, S. V. Morozov, D. Jiang, Y. Zhang, S. V. Dubonos, I. V. Grigorieva, and A. A. Firsov, "Electric field effect in atomically thin carbon films," *Science*, vol. 306, no. 5696, pp. 666–669, 2004.
4. B. Huard, J. A. Sulpizio, N. Stander, K. Todd, B. Yang, and D. Goldhaber-Gordon, "Transport measurements across a tunable

potential barrier in graphene," *Phys. Rev. Lett.*, vol. 98, p. 236803, Jun 2007.
5. J. R. Williams, L. DiCarlo, and C. M. Marcus, "Quantum hall effect in a gate-controlled p-n junction of graphene," *Science*, vol. 317, no. 5838, pp. 638–641, 2007.
6. B. Özyilmaz, P. Jarillo-Herrero, D. Efetov, D. A. Abanin, L. S. Levitov, and P. Kim, "Electronic transport and quantum hall effect in bipolar graphene *p-n-p* junctions," *Phys. Rev. Lett.*, vol. 99, p. 166804, Oct 2007.
7. G. Liu, J. J. Velasco, W. Bao, and C. N. Lau, "Fabrication of graphene p-n-p junctions with contactless top gates," *Appl. Phys. Lett.*, vol. 92, no. 20, p. 203103, 2008.
8. R. V. Gorbachev, A. S. Mayorov, A. K. Savchenko, D. W. Horsell, and F. Guinea, "Conductance of p-n-p graphene structures with air-bridge top gates," *Nano Letters*, vol. 8, no. 7, pp. 1995–1999, 2008, pMID: 18543979.
9. V. V. Cheianov and V. I. Fal'ko, "Selective transmission of Dirac electrons and ballistic magnetoresistance of n-p junctions in graphene," *Phys. Rev. B*, vol. 74, no. 4, p. 041403, JUL 2006.
10. M. I. Katsnelson, K. S. Novoselov, and A. K. Geim, "Chiral tunnelling and the klein paradox in graphene," *Nat. Phys.*, vol. 2, no. 9, p. 620, SEP 2006.
11. N. Stander, B. Huard, and D. Goldhaber-Gordon, "Evidence for klein tunneling in graphene *p-n* junctions," *Phys. Rev. Lett.*, vol. 102, p. 026807, Jan 2009.
12. A. F. Young and P. Kim, "Quantum interference and klein tunnelling in graphene heterojunctions," *Nat. Phys.*, vol. 5, no. 3, pp. 222–226, MAR 2009.
13. S.-G. Nam, D.-K. Ki, J. W. Park, Y. Kim, J. S. Kim, and H.-J. Lee, "Ballistic transport of graphene pnp junctions with embedded local gates," *Nanotechnology*, vol. 22, no. 41, p. 415203, 2011.
14. J. Guo, Y. Yoon, and Y. Ouyang, "Gate electrostatics and quantum capacitance of graphene nanoribbons," *Nano Letters*, vol. 7, no. 7, pp. 1935–1940, 2007.
15. J. Fernández-Rossier, J. J. Palacios, and L. Brey, "Electronic structure of gated graphene and graphene ribbons," *Phys. Rev. B*, vol. 75, p. 205441, May 2007.
16. T. Fang, A. Konar, H. Xing, and D. Jena, "Carrier statistics and quantum capacitance of graphene sheets and ribbons," *Applied Physics Letters*, vol. 91, no. 9, p. 092109, 2007.
17. A. A. Shylau, J. W. Kłos, and I. V. Zozoulenko, "Capacitance of graphene nanoribbons," *Phys. Rev. B*, vol. 80, p. 205402, Nov 2009.
18. T. Andrijauskas, A. A. Shylau, and I. V. Zozoulenko, "Thomas-fermi and poisson modeling of gate electrostatics in graphene nanoribbon," *Lithuanian Journal of Physics*, vol. 52, no. 1, pp. 63–69, 2012.
19. S. Luryi, "Quantum capacitance devices," *Applied Physics Letters*, vol. 52, no. 6, pp. 501–503, 1988.
20. A. V. Shytov, M. S. Rudner, and L. S. Levitov, "Klein backscattering and fabry-pérot interference in graphene heterojunctions," *Phys. Rev. Lett.*, vol. 101, p. 156804, Oct 2008.
21. M.-H. Liu and K. Richter, "Efficient quantum transport simulation for bulk graphene heterojunctions," *Phys. Rev. B*, vol. 86, p. 115455, Sep 2012.
22. V. Krueckl and K. Richter, "Bloch-zener oscillations in graphene and topological insulators," *Phys. Rev. B*, vol. 85, p. 115433, Mar 2012.
23. *Partial Differential Equation Toolbox^{TM} User's Guide*, Matlab 2012a ed., The MathWorks, Inc., 2012.
24. E. I. Rashba, "Properties of semiconductors with an extremum loop i. cyclotron and combinational resonance in a magnetic field perpendicular to the plane of the loop," *Sov. Phys. Solid State*, vol. 2, p. 1109, 1960.
25. Y. A. Bychkov and E. I. Rashba, "Properties of a 2d electron-gas with lifted spectral degeneracy," *JETP Lett.*, vol. 39, p. 78, 1984.
26. M. Gmitra, S. Konschuh, C. Ertler, C. Ambrosch-Draxl, and J. Fabian, "Band-structure topologies of graphene: Spin-orbit coupling effects from first principles," *Phys. Rev. B*, vol. 80, p. 235431, Dec 2009.
27. S. Abdelouahed, A. Ernst, J. Henk, I. V. Maznichenko, and I. Mertig, "Spin-split electronic states in graphene: Effects due to lattice deformation, rashba effect, and adatoms by first principles," *Phys. Rev. B*, vol. 82, p. 125424, Sep 2010.
28. A. Yamakage, K.-I. Imura, J. Cayssol, and Y. Kuramoto, "Interfacial charge and spin transport in Z_2 topological insulators," *Phys. Rev. B*, vol. 83, p. 125401, Mar 2011.
29. H. Y. Tian, Y. H. Yang, and J. Wang, "Interfacial charge current in a magnetised/normal graphene junction," *European Physical Journal B*, vol. 85, no. 8, AUG 2012.
30. A. Yamakage, K. I. Imura, J. Cayssol, and Y. Kuramoto, "Spin-orbit effects in a graphene bipolar pn junction," *EPL*, vol. 87, no. 4, AUG 2009.
31. M.-H. Liu, J. Bundesmann, and K. Richter, "Spin-dependent klein tunneling in graphene: Role of rashba spin-orbit coupling," *Phys. Rev. B*, vol. 85, p. 085406, Feb 2012.
32. M. Rataj and J. Barnaś, "Graphene p-n junctions with nonuniform rashba spin-orbit coupling," *Appl. Phys. Lett.*, vol. 99, no. 16, p. 162107, 2011.
33. J. Sánchez-Barriga, A. Varykhalov, M. R. Scholz, O. Rader, D. Marchenko, A. Rybkin, A. M. Shikin, and E. Vescovo, "Chemical vapour deposition of graphene on Ni(111) and Co(0001) and intercalation with Au to study Dirac-cone formation and Rashba splitting," *Diamond and Related Materials*, vol. 19, no. 7-9, SI, pp. 734–741, JUL-SEP 2010, 20th European Conference on Diamond, Diamond-Like Materials, Carbon Nanotubes and Nitrides, Athens, GREECE, SEP 06-10, 2009.
34. J. Xia, F. Chen, J. Li, and N. Tao, "Measurement of the quantum capacitance of graphene," *Nature Nanotechnology*, vol. 4, no. 8, pp. 505–509, AUG 2009.
35. S. Dröscher, P. Roulleau, F. Molitor, P. Studerus, C. Stampfer, K. Ensslin, and T. Ihn, "Quantum capacitance and density of states of graphene," *Applied Physics Letters*, vol. 96, no. 15, p. 152104, 2010.
36. L. A. Ponomarenko, R. Yang, R. V. Gorbachev, P. Blake, A. S. Mayorov, K. S. Novoselov, M. I. Katsnelson, and A. K. Geim, "Density of states and zero landau level probed through capacitance of graphene," *Phys. Rev. Lett.*, vol. 105, p. 136801, Sep 2010.
37. J. Martin, N. Akerman, G. Ulbricht, T. Lohmann, J. H. Smet, K. Von Klitzing, and A. Yacoby, "Observation of electron-hole puddles in graphene using a scanning single-electron transistor," *Nature Physics*, vol. 4, no. 2, pp. 144–148, FEB 2008.
38. H. Xu, Z. Zhang, and L.-M. Peng, "Measurements and microscopic model of quantum capacitance in graphene," *Applied Physics Letters*, vol. 98, no. 13, p. 133122, 2011.